THE JOURNAL OF BIOLOGICAL CHEMISTRY VOL. 287, NO. 14, pp. 11213–11221, March 30, 2012

Crystal Structure of Perakine Reductase, Founding Member of a Novel Aldo-Keto Reductase (AKR) Subfamily That Undergoes Unique Conformational Changes during NADPH Binding*[S]

Received for publication, December 19, 2011, and in revised form, February 4, 2012 Published, JBC Papers in Press, February 13, 2012, DOI 10.1074/jbc.M111.335521

Lianli Sun[‡], Yixin Chen[‡], Chitra Rajendran[§], Uwe Mueller[¶], Santosh Panjikar[‖], Meitian Wang[§], Rebekka Mindnich[**], Cindy Rosenthal[‡‡], Trevor M. Penning[**], and Joachim Stöckigt[‡1]

From the [‡]Institute of Materia Medica, College of Pharmaceutical Sciences, Zhejiang University, Hangzhou 310058, China, [§]Swiss Light Source PX III, Paul Scherrer Institute, CH-5232 Villigen, Switzerland, [¶]Soft Matter and Functional Materials, Macromolecular Crystallography, BESSY-MX, Elektronenspeicherring BESSY II, D-12489 Berlin, Germany, [‖]Australian Synchrotron, Clayton, Victoria 3168, Australia, the [**]Center of Excellence in Environmental Toxicology and the Department of Pharmacology, University of Pennsylvania School of Medicine, Philadelphia, Pennsylvania 19104-6084, and the [‡‡]Institute of Pharmacy, Department of Pharmaceutical Biology, Johannes Gutenberg-University Mainz, D-55128 Mainz, Germany

Background: Perakine reductase (PR) is an AKR involved in the *Rauvolfia* alkaloid biosynthetic network.
Results: Three-dimensional structures of PR and the A213W mutant complex with NADPH were solved.
Conclusion: PR folds as an unusual α_8/β_6 barrel and undergoes unexpected conformational changes upon NADPH binding.
Significance: PR represents the founding member of the new AKR13D subfamily and provides a structural and cofactor binding template for the AKR13 family.

Perakine reductase (PR) catalyzes the NADPH-dependent reduction of the aldehyde perakine to yield the alcohol raucaffrinoline in the biosynthetic pathway of ajmaline in *Rauvolfia*, a key step in indole alkaloid biosynthesis. Sequence alignment shows that PR is the founder of the new AKR13D subfamily and is designated AKR13D1. The x-ray structure of methylated His_6-PR was solved to 2.31 Å. However, the active site of PR was blocked by the connected parts of the neighbor symmetric molecule in the crystal. To break the interactions and obtain the enzyme-ligand complexes, the A213W mutant was generated. The atomic structure of His_6-PR-A213W complex with NADPH was determined at 1.77 Å. Overall, PR folds in an unusual α_8/β_6 barrel that has not been observed in any other AKR protein to date. NADPH binds in an extended pocket, but the nicotinamide riboside moiety is disordered. Upon NADPH binding, dramatic conformational changes and movements were observed: two additional β-strands in the C terminus become ordered to form one α-helix, and a movement of up to 24 Å occurs. This conformational change creates a large space that allows the binding of substrates of variable size for PR and enhances the enzyme activity; as a result cooperative kinetics are observed as NADPH is varied. As the founding member of the new AKR13D subfamily, PR also provides a structural template and model of cofactor binding for the AKR13 family.

Enzyme-catalyzed biosynthesis and chemo-enzymatic synthesis of pharmacologically active, plant-derived monoterpenoid indole alkaloids have attracted interest in recent years (1–5). A detailed knowledge of the participating enzymes is an indispensable requirement for further progress in this field. One of the largest alkaloid synthetic networks is the *Rauvolfia serpentina* metabolome. In this network we detected perakine reductase, which is involved in a side route of metabolism that branches from the main ajmaline pathway (Fig. 1) and leads to the biosynthesis of dihydroperaksine (6, 7). As an antiarrhythmic drug, ajmaline is well known to act as an antagonist at sodium channels of the heart muscle (8, 9).

Functional overexpression in *Escherichia coli* together with extended substrate studies recently allowed advanced biochemical characterization of PR (6). The NADPH-dependent PR showed a relaxed substrate preference because three groups of structurally diverse compounds were reduced to their corresponding alcohols: two bulky alkaloids, ten medium-sized cinnamic aldehyde derivatives, and four small (nitro)-benzaldehydes (6). In contrast to PR, other enzymes of *Rauvolfia* alkaloid biosynthesis exhibit much higher substrate specificity (10). The absence of both a Rossmann fold (11) and the catalytic motif Tyr-Xaa-Xaa-Xaa-Lys (12) excluded PR as a member of the short chain dehydrogenase/reductase superfamily. However, the presence of a functional catalytic tetrad Asp^{52}, Tyr^{57}, Lys^{84}, and His^{126}, as proven by site-directed mutagenesis, and the presence of other residues highly conserved in aldo-keto reduc-

* This work was supported by funds from Fonds der Chemischen Industrie (Frankfurt/Main, Germany), Deutsche Forschungsgemeinschaft (Bad Godesberg, Germany), Zhejiang University K.P. Chao's Hi-Tech Foundation (Hangzhou, China; to J. S.), and China Postdoctoral Science Foundation Grant 20100471745 (to L. S.).
[S] This article contains supplemental Table S1 and Figs. S1–S5.
The atomic coordinates and structure factors (codes 3UYI and 3V0S) have been deposited in the Protein Data Bank, Research Collaboratory for Structural Bioinformatics, Rutgers University, New Brunswick, NJ (http://www.rcsb.org/).
[1] To whom correspondence should be addressed: Institute of Materia Medica, College of Pharmaceutical Sciences, Zhejiang University, Yuhangtang Rd 388, Hangzhou 310058, China. Tel.: 86-571-88208451; Fax: 86-571-88208449; E-mail: joesto2000@yahoo.com.

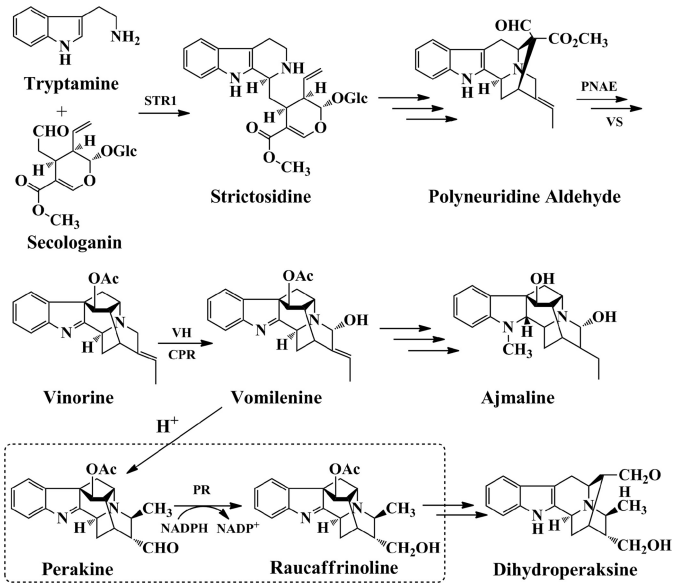

FIGURE 1. **Functional role of PR.** PR is located in a side route branching from the ajmaline biosynthetic pathway leading to dihydroperaksine and extends the metabolic network of *Rauvolfia* monoterpenoid indole alkaloids. (*STR1*, strictosidine synthase, EC 4.3.3.2; *PNAE*, polyneuridine aldehyde esterase, EC 3.1.1.78; *VS*, vinorine synthase, EC 2.3.2.160; *VH*, vinorine hydroxylase, EC 1.14.13.75; *CPR*, cytochrome P450 reductase; H^+ = transformation under acidic conditions).

tase enzymes (AKRs),[2] *i.e.* Gly^{20}, Gly^{47}, Asp^{121}, Pro^{133}, Gly^{154}, Asn^{167}, Pro^{192}, Gln^{196}, and Ser^{252}, indicate affiliation of PR to the AKR enzyme family (13). Furthermore, sequence alignment and preliminary x-ray analysis of a methylated PR mutant support the view that PR represents a novel member of the AKR superfamily (6, 14). In fact, PR would be the first example of a plant AKR involved in indole alkaloid biosynthesis in contrast to the plant AKR-type codeinone reductase, which is involved in isoquinoline alkaloid metabolism (15).

We now describe x-ray analyses of a methylated N-terminal His_6-PR and its A213W mutant complex with the cofactor NADPH. These crystal structures show that PR is an AKR, that it contains an unusual α_8/β_6 barrel, and that it undergoes a novel conformational change upon binding NADPH not seen previously in AKR members. Extended sequence alignment suggests that PR is the founding member of a new AKR13D subfamily.

EXPERIMENTAL PROCEDURES

Protein Expression and Purification—R. serpentina PR cDNA (GenBank™ accession number AY766462) was cloned into pQE-2 vector and expressed as N-terminal His_6-tagged fusion protein in *E. coli* M15 strain (Qiagen). Bacteria were grown at 25 °C for large scale enzyme production, and the conditions for cultivation, induction and purification of recombinant PR were the same as previously reported (6, 14).

Site-directed Mutagenesis—Site-directed mutagenesis was performed to generate the PR-A213W point mutant by using the QuikChange™ site-directed mutagenesis kit (Stratagene, La Jolla, CA). The wild type PR was cloned into pQE-2 as a template, and the following oligonucleotides were used as primers to introduce the mutation: A213W forward primer, 5′-d-GGT CTT TTT **TGG** GGG AAG GCC-3′, and A213W reverse primer, 5′-d-GGC CTT CCC **CCA** AAA AAG ACC-3′.

Protein Methylation—Because of unsuccessful crystallization of native PR, reductive methylation was chosen to modify the protein surface. The purified enzyme was dialyzed against potassium phosphate (KPi) buffer (50 mM, pH 7.0) and concentrated to 10 mg/ml for the subsequent methylation. Methylation was performed by dimethylamine-borane and formaldehyde as previously reported (14, 16).

NADPH Kinetic Behavior—The kinetic properties of NADPH were determined by monitoring product formation by HPLC with seven different NADPH concentrations (2–80 μM) in the presence of substrate (4-nitrobenzaldehyde) (0.2 mM) under standard conditions with 5 μg of purified His_6-PR in KPi buffer (50 mM, pH 7.0) in a total volume of 200 μl. The enzymatic reaction was initiated by adding NADPH. After 15 min of incubation at 30 °C, the reaction was terminated by adding 200 μl of methanol, and the sample was subjected to HPLC to monitor product formation at 254 nm (Waters 2487 detector) with Lichrospher 60 RP-select B column (250 × 4 mm). Acetonitrile/water (1:4, pH 2.3) were used as mobile phase at a flow rate of 1 ml/min.

Size Exclusion Chromatography—Determination of relative molecular weight and oligomerization state of recombinant methylated and unmethylated His_6-PR (6 mg/ml applied) was performed on HiPrep Sephacryl S-200 column using KPi buffer (50 mM, pH 7.0) at a flow rate of 0.5 ml/min. For calibration, the following proteins were used: glucose oxidase (*Aspergillus niger*) (150 kDa), BSA (67 kDa), ovalbumin (45 kDa), and α-chymotrypsin (25 kDa).

Crystallization—Crystallization of methylated His_6-PR was accomplished by the hanging drop vapor diffusion method. The drops were set up by mixing 2 μl of methylated enzyme samples (5.5 mg/ml, 10 mM Tris-HCl buffer, pH 7.0, 1 mM DTT, 10 mM EDTA) with 2 μl of reservoir solution (25% v/v PEG 4000, 0.1 mM sodium citrate, pH 5.6) and equilibrated against 1 ml of reservoir solution at 20 °C for 7 days. Methylated His_6-PR-A213W was also crystallized under the same conditions as methylated His_6-PR.

The crystals of methylated His_6-PR-A213W complex with NADPH were obtained by cocrystallization. Prior to crystallization, the enzyme solutions were incubated with a 3-fold molar excess of NADPH for 2 h at 4 °C to form the complex. The crystallization of the methylated His_6-PR-A213W and NADPH complex was carried out under the same conditions as methylated His_6-PR. The same crystallization conditions were used for the unmethylated His_6-PR-A213W and NADPH complex, with the exception that the enzyme samples were in KPi buffer (50 mM, pH 7.0).

X-ray Data Collection and Processing—All the PR crystals were cryoprotected with 20% glycerol added to the reservoir solution before flash cooling in a stream of nitrogen at 100 K.

Diffraction data of methylated His_6-PR crystals were collected at BW7B beamline at the European Molecular Biology Laboratory Outstation (Hamburg, Germany). The data were

[2] The abbreviations used are: AKR, aldo-keto reductase; PR, perakine reductase; KPi, potassium phosphate; STR1, strictosidine synthase; RMSD, root mean square deviation.

integrated, scaled, and merged with the HKL2000 software package (17). A platinum derivative was derived after the incubation of the methylated His_6-PR crystals with 21% PEG 4000, 0.1 M sodium citrate, pH 5.6, and 10 mM K_2PtCl_4 for 20 min. The multiwavelength anomalous diffraction data collection around the Pt-LIII edge was performed at the MX-beamline BL14–2 of Helmholtz Zentrum Berlin at BESSY II using a SX165 CCD detector (Rayonix, Evanston, IL) and DTB goniostat (Marresearch, Norderstedt, Germany) at 100 K (supplemental Table S1*A*). The data processing was performed by XDS (18).

The crystals of the methylated His_6-PR-A213W, its complex with NADPH, and the unmethylated His_6-PR-A213W complex with NADPH were all measured at PX III beamline at Swiss Light Source (Villigen, Switzerland). Program XDS (18) was applied for data processing.

Structure Solution and Refinement of the Methylated His_6-PR—The crystal structure of the methylated His_6-PR was solved with multiwavelength anomalous diffraction method using the program SHELXC/D/E (19). The initial model (60% of the full structure) was built using RESOLVE (20). This model was used as a starting model in the MRSAD protocol of Auto-Rickshaw (21) against the peak data set for the phase improvement and for the model completion. 85% of the full structure was built automatically. First refinement was performed using REFMAC (22). The model was further improved in several rounds of refinement using automated, restrained refinement with the program PHENIX (23) and by interactive modeling with Coot (24).

Structure Determination of the Methylated/Unmethylated His_6-PR-A213W Complex with NADPH and apo His_6-PR-A213W—The internal processing script at SLS was utilized for initial data processing that uses XDS (18), Labelit (25), MOSFLM (26), and phenix.xtriage (23). Molecular replacement was performed with MOLREP within the CCP4 suite (27) using the refined methylated His_6-PR structure as a search model. The refinement was performed as described above. NADPH was identified in the first electron density map based on the phase of the molecular replacement solution and was included in the model of the methylated and unmethylated His_6-PR-A213W. The refinement statistics are listed in Table 1 and supplemental Table S1*B*. The final model was analyzed with the program MolProbity (28). All of the figures were prepared using PyMOL (29).

Supplemental Data—The following materials are available in the online version of this article: supplemental Table S1*A* showing multiwavelength anomalous diffraction data collection and phasing statistics of methylated His_6-PR, supplemental Table S1*B* showing x-ray data collection and refinement statistics of methylated apo His_6-PR-A213W and unmethylated His_6-PR-A213W complex with NADPH, supplemental Fig. S1 showing residue Ala^{213} of methylated His_6-PR and its nearby region, supplemental Fig. S2 showing size exclusion chromatogram of methylated and unmethylated His_6-PR, supplemental Fig. S3 showing NADPH binding site, supplemental Fig. S4 showing two symmetric holo His_6-PR-A213W molecules in the crystal packing, and supplemental Fig. S5 showing structural comparison of PR and a "generic" AKR to display the diversity in the C terminus.

TABLE 1
PR X-ray data collection and refinement statistics

Structure	mPR[a]	mPR-A213W + NADPH[b]
Data collection		
Wavelength (Å)	0.8148	1.0
Total reflections	213,159	337,656
Unique reflections	16,975	37,054
Mosaicity	0.908	0.183
Resolution (Å)	20-2.31 (2.43-2.31)	48-1.77 (1.82-1.77)
Completeness (%)	96.8 (93.0)	97.6 (80.0)
$I/\sigma(I)$	33.5 (5.4)	49.4 (3.38)
R_{merge} (%)[c]	7.9 (34.9)	4.6 (37.4)
Space group	$C222_1$	$P3_221$
Unit cell (Å)	$a = 58.8$, $b = 93.0$, $c = 143.0$	$a = b = 55.1$, $c = 209.8$
Refinement statistics		
R_{work}[d]/R_{free} (%)[e]	18.9/23.7	19.1/21.1
No. of protein atoms	2480	2227
No. of water molecules	54	358
No. of $NADP^+$ atoms		31
RMSD bond length (Å)	0.015	0.012
RMSD bond angle (°)	1.513	1.494
Average B-factors (Å²)		
Protein	55.3	23.7
Water	50.4	36.6
$NADP^+$		26.8
Ramachandran analysis (%)		
Most favored region	96.7	96.8
Allowed	3.3	3.2
Disallowed	0.0	0.0
Protein Data Bank code	3UYI	3V0S

[a] mPR, methylated His_6-PR wild type.
[b] mPR A213W + NADPH, methylated His_6-PR-A213W complexed with NADPH.
[c] $R_{merge} = |I_i - \langle I_i \rangle| / I_i$, where I_i is the average intensity value of the equivalent reflections.
[d] $R_{work} = \Sigma(|F_o - F_c|)/\Sigma|F_o|$, where F_o and F_c are the observed and calculated structure factors, respectively.
[e] R_{free} was calculated using 5% randomly excluded data from refinement.

RESULTS AND DISCUSSION

Overall Structure of PR—The final three-dimensional structure model of apo methylated PR was derived following refinement of the 2.31 Å data set with 18.9% R_{work} and 23.7% R_{free} (Table 1) and contained 312 amino acid residues and 54 water molecules. There was no defined electron density for two loops, which are residues 26–30 and 221–239.

Methylated apo PR folds into an unusual α/β-barrel consisting unexpectedly of only six β-strands ($\beta1$–$\beta6$) with eight α-helices that pack along the outside of the β-strands (Fig. 2, *A* and *B*). Because of the two missing β-strands, the last two α-helices, $\alpha7$ and $\alpha8$, are directly connected by a loop (Fig. 2*C*). Up to now, all other three-dimensional structures identified for AKR members fold as $(\alpha/\beta)_8$-barrels with eight parallel β-strands and eight α-helices, also known as a triose phosphate isomerase barrel (13, 30). Some typical AKR structural features, such as the β-hairpins (B1 and B2), which cover the top of the barrel at the N terminus, the two helices (H1 and H2), which pack together along the outer barrel, and three large loops (Loops A, B, and C) at the C terminus, are conserved in PR; however, there are also some striking differences when PR is compared with other AKR members (Fig. 2, *C* and *D*). Different from other AKR members, the barrel structure of PR starts with an α-helix instead of a β-strand. In addition, the decoration of the structure with five β-strands, named OOB1–5 (out of bar-

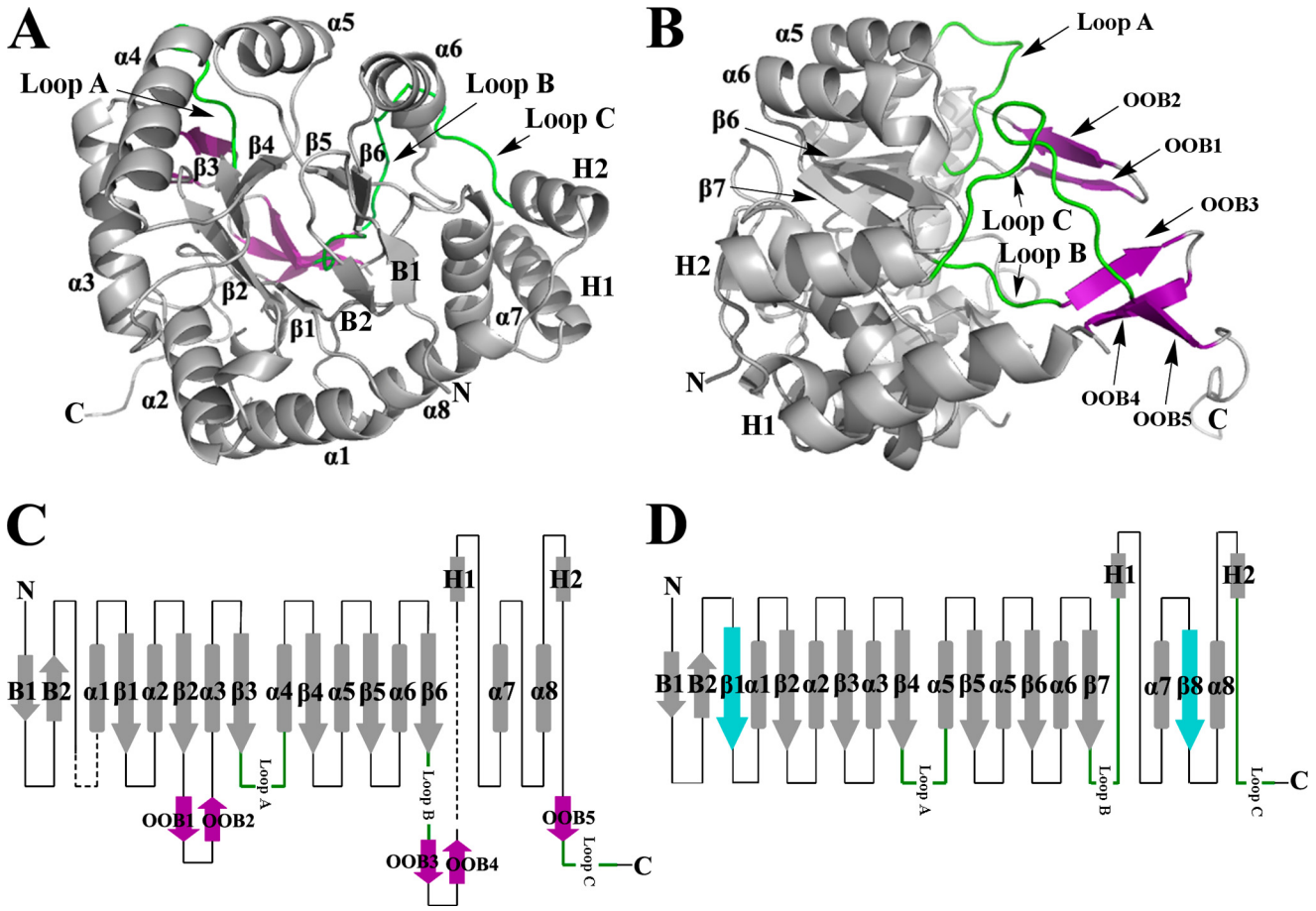

FIGURE 2. **Overall structure of methylated His_6-PR.** *A*, the structure of methylated His_6-PR displays an unusual α_8/β_6 barrel fold for an AKR enzyme. *B*, to show the conformation of OOB1-OOB5 (*purple*) and Loop A–C, Fig. 2*A* is rotated by 90°. The long C-terminal tail is pointing away from the molecule. *C*, topology of the methylated His_6-PR structure. The disordered residues are in *black dashed lines*. *D*, topology of a representative AKR (3α-hydroxysteroid dehydrogenase, AKR1C9). *α1–α8*, the α-helices; *β1–β6*, the β-strands in PR; *β1–β8*, the β-strands in a representative AKR (β1 and β8 (*blue*) are missing in PR); *B1* and *B2*, the two N-terminal β-strands of the hairpin; *H1* and *H2*, the two additional α-helices. The three typical loops (Loops A, B, and C) for AKR enzymes are in *green*. All the other loops are shown as *black lines*. The five additional out of barrel β-strands OOB1–5 at the C terminus are in *purple*. The N and C termini are marked with *N* and *C*.

rel) (Fig. 2*B*), on the C-terminal side is a second notable difference. OOB1–2 are localized between β2 and α3, OOB3–4 are found between Loop B and H1, and OOB5 is directly upstream of Loop C (Fig. 2*C*). Two pairs of these β-strands, OOB1–2 and OOB3–4, form a clamp that covers the C-terminal base of the barrel, whereas the two connecting loops serve as the closing lids. The unique topology of the PR overall architecture is shown in Fig. 2*C*, and the topology of a representative AKR is shown in Fig. 2*D*.

In the asymmetric unit cell there is only one PR molecule, but the two symmetric molecules are strongly connected in the crystal packing (Fig. 3*A*). The interactions between the two molecules occur at their C-terminal regions. The additional five β-strands (OOB1–5), Loop C, and the C-terminal tail appear to be tightly interwoven with a symmetry molecule (Fig. 3*B*) and block the active site (Fig. 3*A*). To break the interactions between the two molecules, the small residue Ala^{213} located in the interface region between the two symmetric molecules was mutated (supplemental Fig. S1 and Fig. 3*B*). A bulky Trp was selected, and the PR-A213W mutant, which is still functional, was generated to prepare PR complexes with cofactor and/or substrate bound.

Two symmetric methylated PR molecules are packed together tightly in the crystal form, but size exclusion studies indicated that methylated PR occurs exclusively as a monomer in solution (supplemental Fig. S2). Moreover, 80% of native (unmethylated) wild type PR seems to exist as a monomer in solution, whereas only 20% are in the dimeric state (supplemental Fig. S2).

Description of PR-Cofactor Complex—The final structure of methylated His_6-PR-A213W complex with NADPH was refined to 1.77 Å resolution to an R_{work} and R_{free} of 19.1% and 21.1%, respectively (Table 1). The model is comprised of 289 amino acids (residues 1–24, 32–219, 243–310, and 328–336), NADPH, and 358 water molecules. Compared with the apo form of PR, there are more disordered residues in the NADPH complex model, especially in the C-terminal region. The strong interactions between the C-terminal residues of the two symmetric molecules found in the crystal packing of the apo form explain the good electron density in this form. Mutation of Ala^{213} to Trp disrupted these interactions and made the cofactor-binding site available for ligand binding. However, in the absence of these intermolecular interactions, some of the C-terminal residues (residues 311–327), which folded as Loop

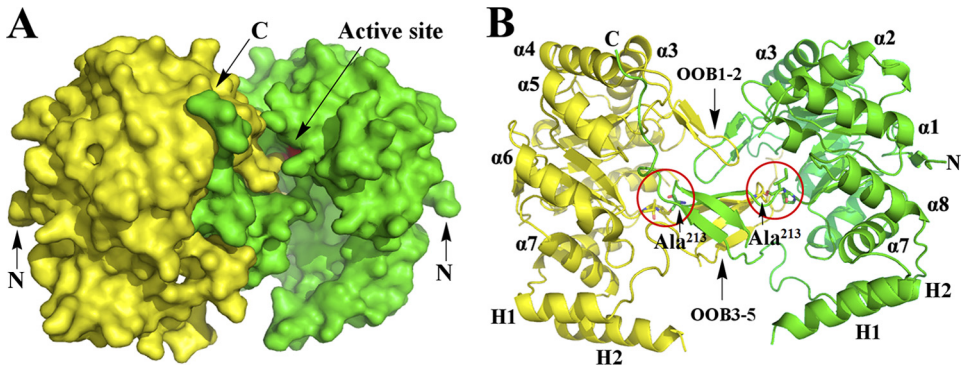

FIGURE 3. **Two symmetric methylated His_6-PR molecules in crystal.** *A*, the two symmetric molecules from the crystal packing are shown in *yellow* and *green* surface presentation. The catalytic tetrad (Asp^{52}, Tyr^{57}, Lys^{84}, and His^{126}) of the molecule is in *red* (*arrow*). *B*, cartoon presentation of *A*. The additional five out of barrel β-strands are grouped together as OOB1–2 and OOB3–5. The N and C termini are marked with *N* and *C*.

C and OOB5 in the apo form, are now more flexible in the new complex, and as such there is insufficient electron density to permit complete structural determination in this region.

For the portion of the PR complex with NADPH that provides a structure, there is similarity in the protein fold with the PR apo form. For example the α_8/β_6 barrel of the two PR forms can be superimposed with RMSD < 0.3 Å, but there are striking differences when the C-terminal regions of both PR forms are compared (Fig. 4). The most significant conformation change occurs from residues 205 to 219. Residues 205–208 reside in Loop B, which is an important part of the cofactor-binding site. Loop B bends inward to the center of the barrel when NADPH is not bound (Fig. 4*A*). However, it points outward and away from the center of the barrel when NADPH is bound. When the two structures are superimposed in this region, an RMSD of the main chains of 2.02 Å with a maximum deviation of 3.94 Å is observed. The similar movement of Loop B is the most frequently observed conformational change in AKRs upon cofactor binding (13, 31, 32).

More severe conformational changes and accompanying movements were observed in the immediate region downstream of Loop B, residues 209–219. The secondary structure in this region contains two β-strands (OOB3–4) with a connecting loop in the apo form, but this changed surprisingly to one α-helix in the NADPH bound (holo) form (Fig. 4*B*). The RMSD of the main chains of this part of the structure between the apo and holo form is 5.73 Å, and the maximum deviation is 12.5 Å. A second AKR enzyme with significant conformational changes induced by NADPH binding is 2,5-diketo-D-gluconic acid reductase A, which shows remarkable structural rearrangements (up to 8 Å) in the catalytic pocket upon cofactor binding accompanied by a switch of an α-helix to an extended β-strand (33). However, the conformational changes discussed herein for PR are significantly more pronounced than those in 2,5-diketo-D-gluconic acid reductase A.

To better illustrate the space produced by this movement, residue Phe^{92} in the connecting loop between OOB1 and OOB2, which is located in the middle of the relatively immobile upper lid of the "clamp" (made of OOB1–2 and OOB3–4), was selected as a marker of a stable position. Residue Gly^{214}, which directly faces Phe^{92}, was selected as a marker of a movable position. The distance between the two C_α atoms of Phe^{92} and Gly^{214} was 6.6 Å in the apo form (Fig. 4*C*), but upon NADPH binding, the distance dramatically increased by ~5-fold to 30.3 Å (Fig. 4*D*). Consequently the "clamp" was completely open. This conformation change creates enough space around the catalytic site for substrate binding, *e.g.* the bulky alkaloids can be accommodated.

To exclude the possibility that mutation Ala^{213} to Trp induces the conformational changes and movements of residues 205–219, the crystallization of apo methylated His_6-PR-A213W was carried out. The x-ray structure of apo methylated His_6-PR-A213W was solved with 2.20 Å resolution (supplemental Table S1*B*). In the absence of the intermolecular interactions that were disrupted by the mutation of Ala^{213} to Trp, the C-terminal segments (residues 205–219 and 311–337) of the apo A213W mutant were much flexible in the crystals, and there is insufficient density for the structure elucidation of above mentioned residues. When NADPH was bound to the A213W mutant, there was clear density corresponding for residues 205–219. The structural difference between apo and holo forms of the mutant indicates that residues 205–219 are involved in cofactor binding. Upon NADPH binding, this part became ordered to form as an α-helix and was fixed to keep the open form and provide enough space for the catalytic reaction to proceed. This observation also confirms that NADPH binding is responsible for the positional and conformational changes.

Crystallography was also performed on the unmethylated His_6-PR-A213W complex with NADPH (supplemental Table S1*B*). The structure obtained at 2.33 Å had a RMSD of 0.7 Å when the methylated and unmethylated PR forms were compared and demonstrates that methylation had no significant influence on the three-dimensional structures.

Binding Mode of NADPH—The cofactor NADPH was bound in the C-terminal core of the barrel of PR and points toward the active site, which is formed by the catalytic tetrad Asp^{52}, Tyr^{57}, Lys^{84}, and His^{126} at the center of the barrel, as in most AKR enzymes (34, 35) (Fig. 5*A*). Because NADPH is easily oxidized to $NADP^+$, the crystal structures of PR complexes likely contain $NADP^+$. However, there was no clear density for the nicotinamide riboside moiety. The final structural model derived from the 1.77 Å diffraction data set clearly defined the binding pattern of this moiety of NADPH in PR (Fig. 5*B* and supplemental Fig. S3). The density (corresponding to the adenine ring, the ribose ring, the adenosine phosphate, and pyrophosphate) of

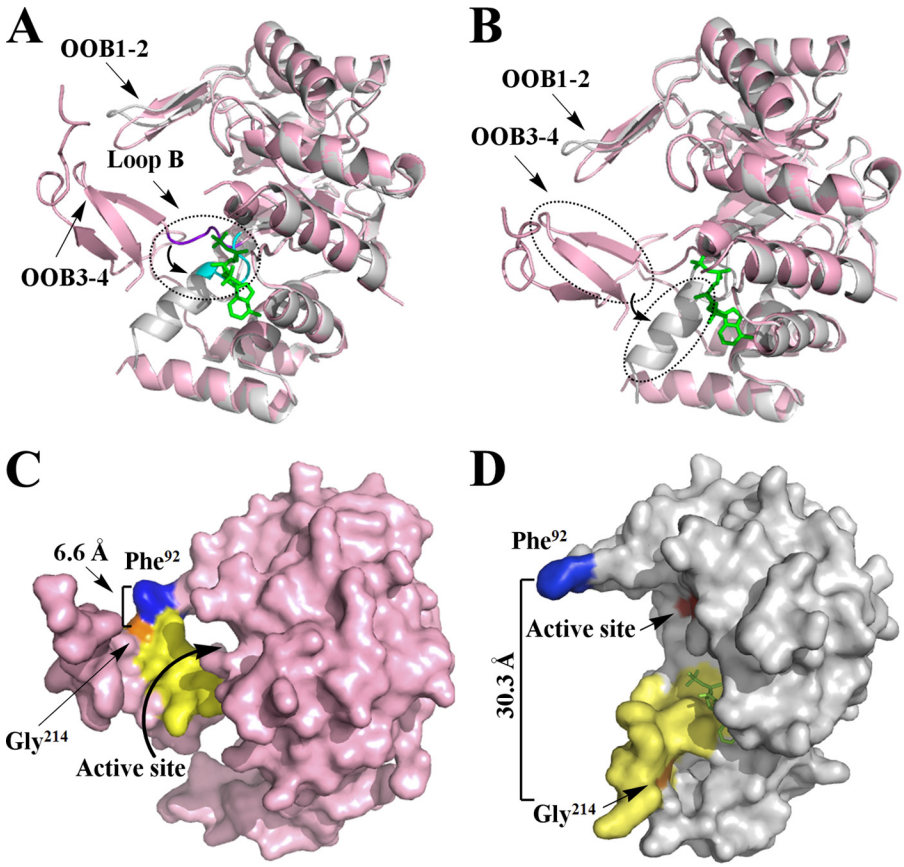

FIGURE 4. **Structure comparison of apo (*pink*) and holo (*gray*) forms of PR.** *A*, superimposed apo and holo forms of PR to show the movement of Loop B upon NADPH binding. Loop B is shown in *purple* in the PR apo form and in *cyan* in the holo form. *B*, superimposed apo and holo forms of PR to show the conformational change and movement of two β-strands (OOB3–4), which switched to one α-helix upon NADPH binding. *C*, surface presentation of the apo form of methylated PR displays the "closed" conformation. *D*, surface presentation of the holo form of methylated PR illustrates the "open" conformation upon NADPH (*green*) binding. The residues that mark protein movement Phe^{92} and Gly^{214}, are in *blue* and *orange*. The residues that change position and conformation (residues 205–219) are in *yellow*. The active site (Asp^{52}, Tyr^{57}, Lys^{84}, and His^{126}) is in *red*.

NADPH lies in an extended groove that stretches from the center to the edge of the barrel and is formed by the surface of residues 205–208 from Loop B, residues 277–282 from the loop linking α7 and α8, and residues 285, 288, and 289 in α8. Many AKR enzymes share a similar mode of cofactor binding across the superfamily (13, 36, 37). However, except for the conservation of Ser^{205} and Asn^{289} in PR, all of the other residues directly hydrogen-bonded with the cofactor are "nonclassical" when compared with other AKR members (Fig. 5, *C* and *D*) (13, 38). As the first example of a structure from the AKR13 family, the PR structural model may provide valuable information on understanding the role of cofactor binding residues across this family.

The disordered nicotinamide riboside portion was therefore modeled in its usual anti-conformation (Fig. 5, *A* and *B*) as seen in other AKR members (36, 39). Sequence alignment shows that several typical AKR cofactor binding residues, *e.g.* Asp^{52}, Ser^{156}, Gln^{176}, and Tyr^{204}, were conserved in PR (Fig. 5, *C* and *D*). These amino acids reside in the space surrounding the active site, and the modeled nicotinamide ring supports their important role in binding the cofactor. The asparagine next to Ser^{156} is strictly conserved in the AKR superfamily and is an important residue in cofactor binding. The hydrogen in δ-N of this asparagine forms a hydrogen bond with the oxygen atom of the carboxamide group in the nicotinamide ring, thereby stabilizing the whole ring. However, in PR this asparagine is replaced by a glutamic acid, which could account for the disorder observed in the binding of the nicotinamide ring.

It is obvious that the cofactor and substrate bind in different regions of the enzyme and converge at the active site. Thereby, the substrate of PR probably occupies the cleft made up of OOB1–2 and the α-helix (switched from OOB3–4). Mutation of A213W completely breaks up the interactions between the OOB3–5, Loop C, and the C-terminal tail and successfully opens the cofactor-binding site, but at the same time, interactions from OOB1–2 still exist. The crystallization pattern of PR complex with NADPH shows that the loop bridging OOB1 and OOB2 from the neighboring molecule partly occupies the active site and the substrate-binding site (supplemental Fig. S4). Our observations may explain why our trials to obtain the ternary complexes of PR, cofactor, and substrates failed.

Kinetics of PR and Structural Changes—PR does not display classical Michaelis-Menten kinetics. When the activity of wild type PR was measured at constant substrate (4-nitrobenzaldehyde) concentration and NADPH concentrations were varied, a sigmoidal velocity (v) *versus* [substrate] plot was obtained (Fig. 6). This result points toward cooperative binding of NADPH (Hill coefficient > 1), which may lead to the enhanced reductase activity of the enzyme. The increase in v may be accounted for the significant conformational change of PR, which we

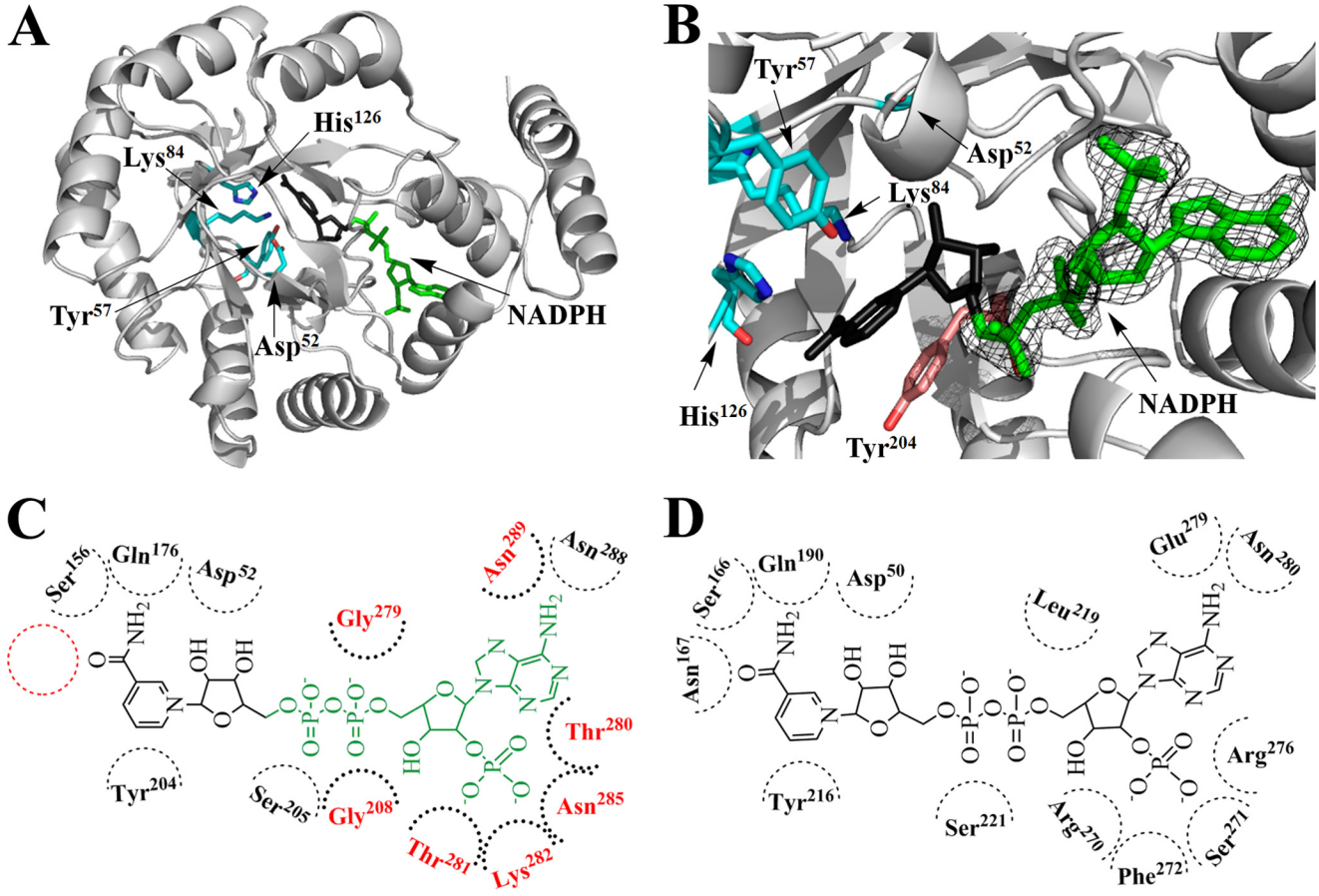

FIGURE 5. **Cofactor binding mode of PR.** *A*, overall structure of methylated His_6-PR-A213W complexed with NADPH (*green*) is shown in a similar orientation as in Fig. 2*A*. The nicotinamide riboside moiety of NADPH (*black*) is disordered in the crystal. The catalytic tetrad (Asp^{52}, Tyr^{57}, Lys^{84}, and His^{126}) is in stick presentation (*cyan*). *B*, a close-up of the catalytic site of methylated His_6-PR-A213W with bound NADPH (*green*). The observed electron density (final $2F_o - F_c$) for NADPH was contoured at 1 σ. Tyr^{204} (*pink*) is the conserved planar aromatic amino acid that in other AKRs stacks with the nicotinamide ring (compared with *A*, rotated by 180°). *C*, NADPH binding in PR. The modeled nicotinamide riboside moiety of NADPH is in *black*. The position of Asn, which is strictly conserved in other AKRs but absent in PR, is shown with a *red circle*. The amino acids which are involved in cofactor binding of PR but differ from the highly conserved amino acids found in other AKRs, are in *red*. *D*, NADPH binding in a typical AKR (3α-hydroxysteroid dehydrogenase) (38).

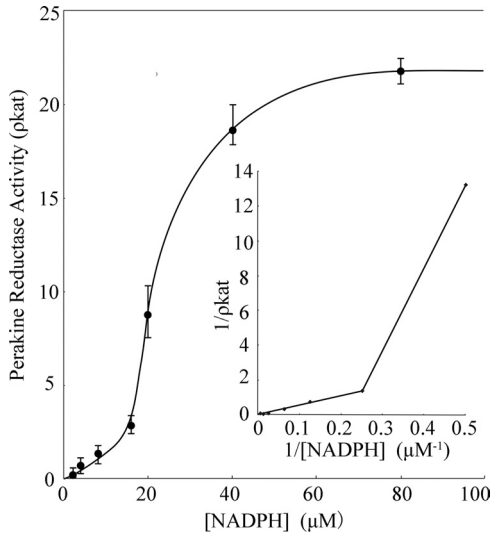

FIGURE 6. **Plot of initial velocity (*v*) *versus* NADPH concentration observed for the reduction of 4-nitrobenzaldehyde catalyzed by PR.**

observed for the NADPH-bound structure (Fig. 4). The cofactor likely opens the entry to the active center of PR, which rapidly and immediately triggers the reduction of the substrate. The NADPH-induced conformational changes are consistent with an ordered bi-bi reaction mechanism, (in which cofactor binds first and leaves last), which is observed in other AKRs (13, 30). Once the second substrate binds, reduction likely utilizes the conserved catalytic tetrad of Tyr, Lys, His, and Asp that lies at the base of the substrate-binding site (40).

Classification and Aspects of Evolution—Multiple sequence alignment and phylogenetic analyses established PR as an AKR13 family member, founding the new subgroup of AKR13D (Fig. 7). PR is also the first plant enzyme in this family that up until now only contained proteins of bacterial and fungal origin. Blast analyses indicate that PR type proteins are absent from the animal kingdom. Furthermore, screening of the NCBI database identified putative PR homologs in a diversity of higher plant species, *e.g. Medicago truncatula*, *Arabidopsis thaliana*, *Oryza sativa*, *Zea mays*, and *Picea sitchensis*. Alignment of *R. serpentina* PR and these putative homologs showed high sequence conservation with ~70% of the residues being identical. In comparison, strictosidine synthase (STR1), the first enzyme in the biosynthetic pathway to monoterpenoid indole alkaloids (Fig. 1) (41), appears to be far less conserved. Sequence identity between well characterized *Rauvolfia* STR1 and its putative homologs in the species listed above was only

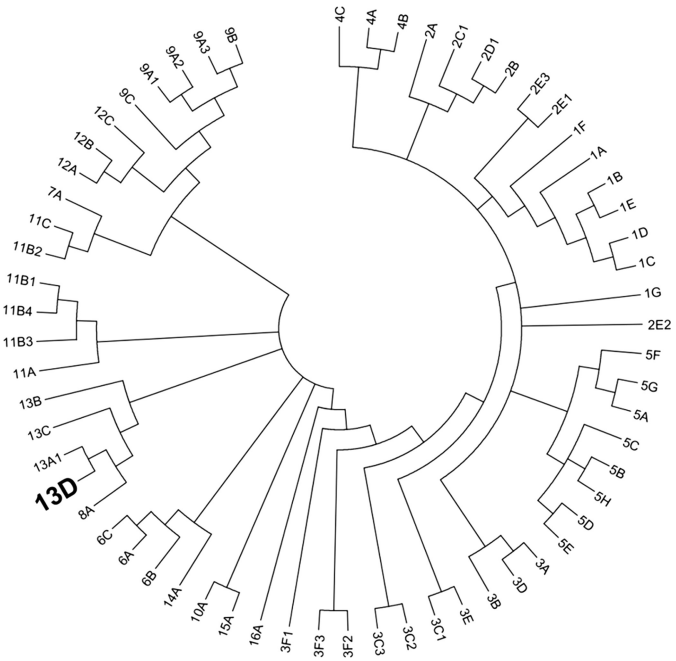

FIGURE 7. **Evolutionary relationship of new AKR13D from *R. serpentina* to annotated AKR families and subfamilies.** The dendrogram shows the topological relationships between AKR subfamilies. The new AKR13D from *R. serpentina* is most closely related to other members of the AKR13 family and AKR8. The evolutionary history of all annotated AKRs including the new AKR from *R. serpentina* was inferred using the neighbor joining method (43). A bootstrap consensus tree was inferred from 1000 replicates (44), with subfamily branches collapsed where possible. Branches corresponding to partitions reproduced in less than 30% bootstrap replicates were also collapsed. The evolutionary distances were computed using the Poisson correction method (45) and are in the units of the number of amino acid substitutions per site. All of the positions containing alignment gaps and missing data were eliminated only in pairwise sequence comparisons (pairwise deletion option). There were a total of 607 positions in the final data set. Phylogenetic analyses were conducted in MEGA4 (46).

~40%. However, because of the high sequence diversity of proteins such as STR1 that feature a six-bladed β-propeller structure and their lack of functional characterization, these putative homologous proteins identified *in silico* may not be functional STR1 orthologs (42). Consequently, STR1 and the strictosidine pathway would be absent in those species that otherwise seem to harbor a well conserved PR. These observations and the wide spectrum of PR substrates (6) suggest that although PR is involved in the secondary metabolism of strictosidine in *Rauvolfia*, it may play additional roles in other well conserved biosynthesis pathways in higher plants.

Acknowledgments—We thank Dr. Yi Jin (Research Assistant Professor at the Perleman School of Medicine) for a careful read of the manuscript. We thank the staff members of Shanghai Synchrotron Radiation Facility.

REFERENCES

1. Ruppert, M., Ma, X., and Stöckigt, J. (2005) Alkaloid biosynthesis in *Rauvolfia*-cDNA cloning of major enzymes of the ajmaline pathway. *Curr. Org. Chem.* **9,** 1431–1444
2. Lee, H. Y., Yerkes, N., and O'Connor, S. E. (2009) Aza-tryptamine substrates in monoterpene indole alkaloid biosynthesis. *Chem. Biol.* **16,** 1225–1229
3. Runguphan, W., Qu, X., and O'Connor, S. E. (2010) Integrating carbon-halogen bond formation into medicinal plant metabolism. *Nature* **468,** 461–464
4. Loris, E. A., Panjikar, S., Ruppert, M., Barleben, L., Unger, M., Schübel, H., and Stöckigt, J. (2007) Structure-based engineering of strictosidine synthase: auxiliary for alkaloid libraries. *Chem. Biol.* **14,** 979–985
5. Zou, H. B., Zhu, H. J., Zhang, L., Yang, L. Q., Yu, Y. P., and Stöckigt, J. (2010) A facile chemoenzymatic approach: one-step syntheses of monoterpenoid indole alkaloids. *Chem. Asian J.* **5,** 2400–2404
6. Sun, L., Ruppert, M., Sheludko, Y., Warzecha, H., Zhao, Y., and Stöckigt, J. (2008) Purification, cloning, functional expression and characterization of perakine reductase: the first example from the AKR enzyme family, extending the alkaloidal network of the plant *Rauvolfia*. *Plant Mol. Biol.* **67,** 455–467
7. Edwankar, R. V., Edwankar, C. R., Deschamps, J., and Cook, J. M. (2011) Regiospecific, enantiospecific total synthesis of C-19 methyl substituted sarpagine alkaloids dihydroperaksine-17-al and dihydroperaksine. *Org. Lett.* **13,** 5216–5219
8. Cordell, G. A. (1981) *Introduction to Alkaloids: A Biogenetic Approach*, John Wiley and Sons, New York
9. Kiesecker, C., Zitron, E., Lück, S., Bloehs, R., Scholz, E. P., Kathöfer, S., Thomas, D., Kreye, V. A. W., Katus, H. A., Schoels, W., Karle, C. A., and Kiehn, J. (2004) Class la anti-arrhythmic drug ajmaline blocks HERG potassium channels: model of action. *Naunyn-Schmiedebergs Arch. Pharmacol.* **370,** 423–435
10. Yang, L., Hill, M., Wang, M., Panjikar, S., and Stöckigt, J. (2009) Structural basis and enzymatic mechanism of the biosynthesis of C_9 from C_{10} monoterpenoid indole alkaloids. *Angew. Chem. Int. Ed. Engl.* **48,** 5211–5213
11. Rao, S. T., and Rossmann, M. G. (1973) Comparison of super-secondary structures in proteins. *J. Mol. Biol.* **76,** 241–256
12. Persson, B., Krook, M., and Jörnvall, H. (1991) Characteristics of short-chain alcohol dehydrogenases and related enzymes. *Eur. J. Biochem.* **200,** 537–543
13. Jez, J. M., Bennett, M. J., Schlegel, B. P., Lewis, M., and Penning, T. M. (1997) Comparative anatomy of the aldo-keto reductase superfamily. *Biochem. J.* **326,** 625–636
14. Rosenthal, C., Mueller, U., Panjikar, S., Sun, L., Ruppert, M., Zhao, Y., and Stöckigt, J. (2006) Expression, purification, crystallization and preliminary x-ray analysis of perakine reductase, a new member of the aldo-keto reductase enzyme superfamily from higher plants. *Acta Crystallogr. Sect. F Struct. Biol. Cryst. Commun.* **62,** 1286–1289
15. Unterlinner, B., Lenz, R., and Kutchan, T. M. (1999) Molecular cloning and functional expression of codeinone reductase: the penultimate enzyme in morphine biosynthesis in the opium poppy *Papaver somniferum*. *Plant J.* **18,** 465–475
16. Rypniewski, W. R., Holden, H. M., and Rayment, I. (1993) Structural consequences of reductive methylation of lysine residues in hen egg white lysozyme. An X-ray analysis at 1.8-. ANG. resolution. *Biochemistry* **32,** 9851–9858
17. Otwinowski, Z., and Minor, W. (1997) Processing of x-ray diffraction data collected in oscillation mode. *Methods Enzymol.* **276,** 307–326
18. Kabsch, W. (1993) Automatic processing of rotation diffraction data from crystals of initially unknown symmetry and cell constants. *J. Appl. Crystallogr.* **26,** 795–800
19. Sheldrick, G. M. (2002) Macromolecular phasing with SHELXE. *Z. Kristallogr* **217,** 644–650
20. Terwilliger, T. C. (2000) Maximum-likelihood density modification. *Acta Crystallogr. D Biol. Crystallogr.* **56,** 965–972
21. Panjikar, S., Parthasarathy, V., Lamzin, V. S., Weiss, M. S., and Tucker, P. A. (2005) Auto-rickshaw: an automated crystal structure determination platform as an efficient tool for the validation of an X-ray diffraction experiment. *Acta Crystallogr. D Biol. Crystallogr.* **61,** 449–457
22. Murshudov, G. N., Vagin, A. A., and Dodson, E. J. (1997) Refinement of macromolecular structures by the maximum-likelihood method. *Acta Crystallogr. D Biol. Crystallogr.* **53,** 240–255
23. Adams, P. D., Grosse-Kunstleve, R. W., Hung, L. W., Ioerger T. R., McCoy, A. J., Moriarty, N. W., Read, R. J., Sacchettini, J. C., Sauter, N. K., and Terwilliger, T. C. (2002) PHENIX: building new software for automated

crystallographic structure determination. *Acta Crystallogr. D Biol. Crystallogr.* **58,** 1948–1954
24. Emsley, P., and Cowtan, K. (2004) Coot: model-building tools for molecular graphics. *Acta Crystallogr. D Biol. Crystallogr.* **60,** 2126–2132
25. Sauter, N. K., and Poon, B. K. (2010) Autoindexing with outlier rejection and identification of superimposed lattices. *J. Appl. Crystallogr.* **43,** 611–616
26. Leslie, A. G. W. (2006) The integration of macromolecular diffraction data. *Acta Crystallogr. D Biol. Crystallogr.* **62,** 48–57
27. Potterton, L., McNicholas, S., Krissinel, E., Gruber, J., Cowtan, K., Emsley, P., Murshudov, G. N., Cohen, S., Perrakis, A., and Noble, M. (2004) Developments in the CCP4 molecular-graphics project. *Acta Crystallogr. D Biol. Crystallogr.* **60,** 2288–2294
28. Davis, I. W., Leaver-Fay, A., Chen, V. B., Block, J. N., Kapral, G. J., Wang, X., Murray, L. W., Arendall, W. B., 3rd, Snoeyink, J., Richardson J. S., and Richardson, D. C., (2007) MolProbity: all-atom contacts and structure validation for proteins and nucleic acids. *Nucleic Acids Res.* **35,** W375–W383
29. DeLano W. L. (2002) *The PyMOL Molecular Graphics System,* DeLano Scientific, San Carlos, CA, U.S.A.
30. Jin, Y., and Penning, T. M. (2007) Aldo-keto reductases and bioactivation/detoxication. *Annu. Rev. Pharmacol. Toxicol.* **47,** 263–292
31. Richter, N., Breicha, K., Hummel, W., and Niefind, K. (2010) The three-dimensional structure of AKR11B4, a glycerol dehydrogenase from *Gluconobacter oxydans*, reveals a tryptophan residue as an accelerator of reaction turnover. *J. Mol. Biol.* **404,** 353–362
32. Olsen, J. G., Pedersen, L., Christensen, C. L., Olsen, O., and Henriksen, A. (2008) Barley aldose reductase: structure, cofactor binding, and substrate recognition in the aldo/keto reductase 4C family. *Proteins* **71,** 1572–1581
33. Sanli, G., and Blaber, M. (2001) Structural assembly of the active site in an aldo-keto reductase by NADPH cofactor. *J. Mol. Biol.* **309,** 1209–1218
34. Simpson, P. J., Tantitadapitak, C., Reed, A. M., Mather, O. C., Bunce, C. M., White, S. A., and Ride, J. P. (2009) Characterization of two novel aldo-keto reductases from *Arabidopsis*: expression patterns, broad substrate specificity, and an open active-site structure suggest a role in toxicant metabolism following stress. *J. Mol. Biol.* **392,** 465–480
35. Scoble, J., McAlister, A. D., Fulton, Z., Troy, S., Byres, E., Vivian, J. P., Brammananth, R., Wilce, M. C. J., Le Nours, J., Zaker-Tabrizi, L., Coppel, R. L., Crellin, P. K., Rossjohn, J., and Beddoe, T. (2010) Crystal structure and comparative functional analyses of a *Mycobacterium* aldo-keto reductase. *J. Mol. Biol.* **398,** 26–39
36. Sundaram, K., Dhagat, U., Endo, S., Chung, R., Matsunaga, T., Hara, A., and El-Kabbani, O. (2011) Structure of rat aldose reductase-like protein AKR1B14 holoenzyme: probing the role of His269 in coenzyme binding by site-directed mutagenesis. *Bioorg. Med. Chem. Lett.* **21,** 801–804
37. Di Costanzo, L., Drury, J. E., Penning, T. M., and Christianson, D. W. (2008) Crystal structure of human liver Δ4–3-ketosteroid 5β-reductase (AKR1D1) and implications for substrate binding and catalysis. *J. Biol. Chem.* **283,** 16830–16839
38. Bennett, M. J., Schlegel, B. P., Jez, J. M., Penning, T. M., and Lewis, M. (1996) Structure of 3α-hydroxysteroid/dihydrodiol dehydrogenase complexed with $NADP^+$. *Biochemistry* **35,** 10702–10711
39. Faucher, F., Pereira de Jésus-Tran, K., Cantin, L., Luu-The, V., Labrie, F., and Breton, R. (2006) Crystal structures of mouse 17α-hydroxysteroid dehydrogenase (apoenzyme and enzyme-NADP(H) binary complex): identification of molecular determinants responsible for the unique 17α-reductive activity of this enzyme. *J. Mol. Biol.* **364,** 747–763
40. Schlegel, B. P., Jez, J. M., Penning, T. M. (1998) Mutagenesis of 3α-hydroxysteroid dehydrogenase reveals a "push-pull" mechanism for proton transfer in aldo-keto reductases. *Biochemistry* **37,** 3538–3548
41. Stöckigt, J., Barleben, L., Panjikar, S., and Loris, E. A. (2008) 3D-Structure and function of strictosidine synthase: the key enzyme of monoterpenoid indole alkaloid biosynthesis. *Plant Physiol. Biochem.* **46,** 340–355
42. Hicks, M. A., Barber, A. E., 2nd, Giddings, L. A., Caldwell, J., O'Connor, S. E., and Babbitt, P. C. (2011) The evolution of function in strictosidine synthase-like proteins. *Proteins* **79,** 3082–3098
43. Saitou, N., and Nei, M. (1987) The neighbor-joining method: a new method for reconstructing phylogenetic trees. *Mol. Biol. Evol.* **4,** 406–425
44. Felsenstein, J. (1985) Confidence limits on phylogenies: an approach using the bootstrap. *Evolution* **39,** 783–791
45. Zuckerkandl, E., and Pauling, L. (1965) "Evolutionary divergence and convergence in proteins," in *Evolving Genes and Proteins*, pp. 97–166, Academic Press, New York
46. Tamura, K., Dudley, J., Nei, M., and Kumar, S. (2007) MEGA4: molecular Evolutionary Genetics Analysis (MEGA) software version 4.0. *Mol. Biol. Evol.* **24,** 1596–1599